Available online at www.sciencedirect.com
SCIENCE DIRECT®
International Journal of Multiphase Flow 30 (2004) 1485–1508
International Journal of Multiphase Flow
www.elsevier.com/locate/ijmulflow

Direct numerical simulations of two-layer viscosity-stratified flow

Qing Cao, Kausik Sarkar, Ajay K. Prasad *

Department of Mechanical Engineering, University of Delaware, 126 Spencer Lab, Newark, DE 19716, USA

Received 16 May 2003; received in revised form 28 July 2004

Abstract

Two-dimensional simulations of flow instability at the interface of a two-layer, density-matched, viscosity-stratified Poiseuille flow are performed using a front-tracking/finite difference method. We present results for the small-amplitude (linear) growth rate of the instability at small to medium Reynolds number for varying thickness ratio n, viscosity ratio m, and wavenumber. We also present results for large-amplitude non-linear evolution of the interface for varying viscosity ratio and interfacial tension. For the linear case, the interfacial mode is neutrally stable for $n = \sqrt{m}$ as predicted by analysis. The growth rate is proportional to Reynolds number for small Re, and increases with viscosity ratio. The growth rate also increases when the thickness of the more viscous layer is reduced. Strong non-linear behavior is observed for relatively large initial perturbation amplitude. The higher viscosity fluid is drawn out as a finger that penetrates into the lower viscosity layer. The simulated interface shape compares well with previously reported experiments. Increasing interfacial tension retards the growth rate of the interface as expected, whereas increasing the viscosity ratio enhances it. Drop formation at the small Reynolds number considered in this study is precluded by the two-dimensional nature of the calculations.

Keywords: Viscosity-stratified flow; Direct numerical simulations; Front tracking; Linear stability; Non-linear stability; Finger formation

* Corresponding author. Tel.: +1 302 831 2960; fax: +1 302 831 3619.
E-mail address: prasad@me.udel.edu (A.K. Prasad).

0301-9322/$ - see front matter © 2004 Elsevier Ltd. All rights reserved.
doi:10.1016/j.ijmultiphaseflow.2004.07.005

1. Introduction

Two-layer viscosity-stratified flow has been a topic of many theoretical investigations, and a brief review is presented here. Yih (1967) used a long-wave perturbation analysis to show that two-layer, viscosity-stratified plane Poiseuille flow and plane Couette flow can be unstable for arbitrarily small Reynolds numbers. The growth rate was found to be proportional to $\alpha^2 Re$, where α is the dimensionless wavenumber and Re is the Reynolds number. Hickox (1971) applied Yih's method to axisymmetric vertical pipe flow of two fluids with different densities wherein the core is less viscous than the annulus, and concluded that the primary flow was always unstable to either asymmetric or axisymmetric disturbances, and second, that the instability was primarily due to viscosity stratification. Joseph et al. (1984) extended Hickox's study by considering lubricated pipelining in which the core is more viscous than the annulus. They showed that lubricated flows could be stabilized by carefully choosing the flow parameters.

Yiantsios and Higgins (1988) extended Yih's (1967) study of two-layer viscosity-stratified plane Poiseuille flow by adding interfacial tension and density differences, and by considering small and large wavenumbers. Asymptotic analyses were supplemented with numerical solutions of the Orr–Sommerfeld equations. Neutral stability curves were calculated for a wide parameter range. Both interfacial and shear mode instabilities were investigated, and theoretical predictions for the critical Reynolds numbers for both modes were compared with experiments.

Renardy and Joseph (1985) investigated the stability of Couette flow of two immiscible fluids between concentric cylinders using a short wave asymptotic analysis. They found that, in the absence of interfacial tension, centrifugal forces would produce a stable flow if the denser fluid were outside. Under certain conditions, if interfacial tension is large enough to stabilize the short waves but not so large that the long waves are unstable, then stability is possible at all wave parameters with the denser fluid inside. They showed that Taylor instability for a one-fluid flow may be delayed by the addition of a thin layer of less-viscous fluid on the inner wall, and promoted by a thin layer of more-viscous fluid on the inner wall.

Charru and Fabre (1994) considered plane Couette–Poiseuille flow of two layers of viscous fluids with moderate interfacial tension by a second order perturbation method. For $Re = O(1)$, Poiseuille flow was found to be stable against long wavelength disturbances if and only if the primary flow was convex, a result consistent with Hickox (1971). Second, stable Couette flow could become unstable when the Reynolds number of one fluid was decreased, implying that inertia might stabilize low–Re instability.

South and Hooper (1999) re-examined linear stability of two-fluid plane Poiseuille flow concentrating on transient growth and its dependence on viscosity and depth ratio. They stated that because the interfacial mode is usually the leading eigenmode, linear stability studies to date have focused on the interfacial mode, and non-linear studies have focused on the reaction of the interfacial mode to finite-amplitude disturbances. On the other hand, their study recognized the importance of non-normality in the Orr–Sommerfeld equation, and considered disturbances defined as the sum of the least stable eigenmodes and not just the least stable interfacial mode.

Renardy (1989) studied the *non-linear* stability of two-layer Couette–Poiseuille flow with interfacial tension using bifurcation theory. Neutral stability curves were presented for several situations at low Reynolds number, and the results were compared with those derived from the long wave asymptotic method. The neutral curves tend to move toward the curves of long waves

when the surface tension is increased. The critical wavenumbers for several specific situations were also derived in the paper.

In contrast to the large number of theoretical investigations, relatively few experimental studies have addressed the problem of multi-layer viscosity-stratified flow. Recently, Khomami and Su (2000) observed viscous interfacial instabilities for the first time in experiments on two-layer plane Poiseuille flows with small interfacial tension. They showed that the growth rate of interfacial disturbances was indeed linear and obtained good quantitative agreement with theoretical predictions. Khomami et al. (2000) compared results from experiments of pressure-driven channel flow of two fluids with linear and weakly non-linear theory. Sangalli et al. (1995) compared experimental results of instability in a two-layer viscosity stratified rotating Couette flow with weakly non-linear theory. Cao et al. (2003) performed an experimental investigation of an axisymmetric viscosity-stratified flow with vanishing interfacial tension using laser induced fluorescence (LIF) and particle image velocimetry (PIV). A comparison of experimental stable cases and exact solutions revealed the existence of a thin interfacial layer which smoothes out the discontinuity of the velocity gradient at the interface. They also observed two kinds of unstable modes for the first time: (1) wavy core-flow with fissures, and (2) wavy core-flow with core breakup. The results confirmed that viscosity stratification can cause instabilities even when the Reynolds number is O(1). The results of time-averaged experimental velocity profiles for the unstable case indicated a broadening of the core flow, which was consistent with the LIF visualization.

The typical procedure for most of the analytical studies listed above is to start with the Navier–Stokes equations, introduce a perturbation on the primary motion, derive the Orr–Sommerfeld equations, and solve them using a suitable numerical method. Direct numerical solutions (DNS) of the Navier–Stokes equations are difficult due to the unsteady evolution of the interface between dissimilar fluids, implying that the interface shape must be determined concurrently using equations that are coupled with the Navier–Stokes equations. Such a numerical solution is particularly attractive because it does not face constraints that are typical in analytical treatments, such as linearity and small-amplitude perturbations. For example, DNS calculations using the volume of fluid (VOF) method for two-layer Couette flow by Coward et al. (1997) showed that the interface evolves to form waves with a steep front for certain parameter regimes. Subsequently, finger formation at the interface in the non-linear regime was presented for the same problem by Li et al. (1998) and Renardy and Li (1999) also using the VOF method.

The front-tracking/finite difference method was originally formulated by Unverdi and Tryggvason (1988) and Esmaeeli and Tryggvason (1998, 1999). Recently Sarkar and Schowalter (2001a,b) used it to study drop deformation in time dependent flows at finite Reynolds numbers. They also developed a viscoelastic code and studied a drop of upper-convected Maxwell liquid deforming in a similar flow field (Sarkar and Schowalter, 2002). Zhang et al. (2002) applied the method to a gravity driven two-layer fluid flow in an inclined channel. A growing finger was observed at the interface under certain conditions. The front-tracking method was also applied by Tauber et al. (2002) to conduct calculations on the Kelvin–Helmholtz stability of an interface between two immiscible fluids. The front-tracking method offers greater generality over boundary element methods, and is an attractive alternative to finite difference (with a body-fitted coordinate system) or finite element implementations.

In this paper, we investigate the instability at the interface of two fluids in a Poiseuille channel flow. Sections 2 and 3 describe the mathematical formulation of the problem and its numerical

implementation. Results from a detailed two-dimensional computation are presented for different parameters in Section 4. We first apply the method to study the response of the interface with vanishing interfacial tension to small disturbances and confirm that our results are in good agreement with theoretical predictions summarized in the preceding paragraphs. Next, we extend the study to the highly non-linear regime and obtain new and interesting results for large interfacial amplitude evolution for varying viscosity ratio and interfacial tension. The relevant parameters are systematically varied and the effects collated and explained. We summarize our findings in Section 5.

2. Mathematical formulation

2.1. Governing equations

The velocity field $\boldsymbol{u}$ and the pressure p satisfy the equation of momentum conservation

$$\frac{\partial(\rho \boldsymbol{u})}{\partial t} + \nabla \cdot (\rho \boldsymbol{u}\boldsymbol{u}) = -\nabla p - \int_{\partial B} \mathrm{d}\boldsymbol{x}_B \kappa \boldsymbol{n} \sigma \delta(\boldsymbol{x} - \boldsymbol{x}_B) + \nabla \cdot \mu[\nabla \boldsymbol{u} + (\nabla \boldsymbol{u})^{\mathrm{T}}], \tag{1}$$

in the entire domain consisting of the two continuous fluid domains Ω_1 and Ω_2 (Fig. 1). Here σ is the interfacial tension, ∂B is the interface (front) consisting of points $\boldsymbol{x}_B$, κ the local curvature, $\boldsymbol{n}$ the normal to the surface, $\delta(\boldsymbol{x} - \boldsymbol{x}_B)$ is the Dirac delta function (two-dimensional for the present problem), μ is the viscosity, and the superscript T represents the transpose of the velocity gradient $\nabla \boldsymbol{u}$. Interfacial tension produces a jump in the normal stress across the interface, and is represented as a (singular) distributed body force, anticipating its numerical implementation to be described below. Note that, we set the interfacial tension to zero for the linear results in this paper, whereas the interfacial tension was varied for the non-linear cases. The flow field is incompressible with density ρ,

$$\nabla \cdot \boldsymbol{u} = 0. \tag{2}$$

Note that the velocity field satisfies a single equation in both phases with a spatially varying viscosity $\mu(\boldsymbol{x}, t)$ that satisfies

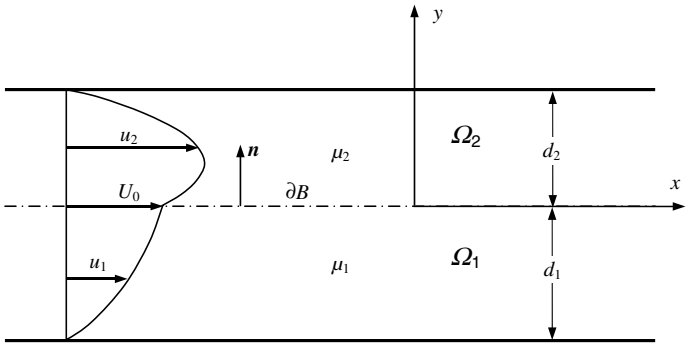

Fig. 1. Flow geometry under consideration.

$$\frac{D\mu}{Dt} \equiv \frac{\partial \mu}{\partial t} + \boldsymbol{u} \cdot \nabla \mu = 0. \tag{3}$$

Moreover, by applying the momentum Eq. (1) in a rectangular element of vanishing thickness straddling the front, one can recover velocity and shear stress continuity across the front, and the jump in the normal stress due to interfacial tension.

2.2. Geometry and initial conditions

Fig. 1 depicts the two-dimensional flow geometry under consideration. We consider two liquids that are co-flowing in a channel. The lower liquid has a thickness d_1, with a volume flux Q_1 and viscosity μ_1. The upper liquid has a thickness d_2, with a volume flux Q_2 and viscosity μ_2.

We use the velocity profile of the primary flow as the initial velocity field. The primary flow has only one non-zero velocity component, which is a function of the vertical co-ordinate y. The corresponding steady-flow governing equation is

$$\frac{d^2u}{dy^2} = \frac{1}{\mu}\frac{dp}{dx}. \tag{4}$$

The relevant boundary conditions are no-slip at the wall, velocity continuity at the interface, and continuity of shear stress at the interface. We define the thickness ratio as $n = d_1/d_2$, and the viscosity ratio as $m = \mu_1/\mu_2$.

Eq. (4) is easily solved to yield:

$$\frac{u_1}{U_0} = 1 + \frac{m - n^2}{m(n^2 + n)}\frac{y}{d_2} - \frac{m + n}{m(n^2 + n)}\left(\frac{y}{d_2}\right)^2, \tag{5}$$

$$\frac{u_2}{U_0} = 1 + \frac{m - n^2}{(n^2 + n)}\frac{y}{d_2} - \frac{m + n}{n^2 + n}\left(\frac{y}{d_2}\right)^2, \tag{6}$$

where U_0 is the interfacial velocity given by

$$U_0 = -\frac{1}{2}\frac{dp}{dx}\frac{d_1 d_2}{\mu_2}\frac{n+1}{m+n}. \tag{7}$$

2.3. Boundary conditions

The boundary conditions are no-slip at the upper and the lower walls. Periodic boundary conditions are applied at the inlet and outlet region to simulate the spatially evolving flow.

2.4. Interface

The velocity at a point on the interface $\boldsymbol{u}(\boldsymbol{x_B})$ is related to the field velocity using the property of the delta function:

$$\boldsymbol{u}(\boldsymbol{x}_B) = \int_\Omega \mathrm{d}\boldsymbol{x}\delta(\boldsymbol{x} - \boldsymbol{x}_B)\boldsymbol{u}(\boldsymbol{x}). \tag{8}$$

As noted earlier, the interface conditions of stress and velocity continuities are automatically met by the governing equation with spatially varying viscosities and the distributed forces (due to interfacial tension) in the field equation.

For most of the simulations, we introduce a sinusoidal perturbation at the interface, $y = +a_0\cos(2\pi x/\lambda)$, where y is the vertical position of the interface, a_0 is the initial amplitude of the perturbation, x is the downstream distance, and λ is the wavelength. This single sine wave perturbation closely corresponds to the most dangerous mode as will be demonstrated subsequently.

3. Numerical implementation

The physical domain is represented numerically as a box of size L_x and L_y. We have used $L_x = L_y = d_1 + d_2$ and a 64×64 grid unless otherwise mentioned. The interface between the two fluids is described by line elements. Initially the elements are created by placing points on the line. The movement of the element vertices describes the evolving shape of the interface. An adaptive regridding scheme is implemented to prevent the elements from distorting excessively. The scheme creates/destroys elements by insertion/removal of points on the existing front.

3.1. Front tracking

The properties of the upper fluid (such as μ_2 and ρ_2) could be different from those in the lower fluid. The current simulations are for density-matched liquids. The conventional approach for such problems involves solving a set of governing equations for each fluid, and matching them at the interface. The present method reduces the two layers to a single layer with spatially varying properties, and thereby eliminates the explicit matching at the interface. For this purpose, the material properties are written as

$$\mu(\boldsymbol{x}) = \mu_2 + (\mu_1 - \mu_2)I(\boldsymbol{x}). \tag{9}$$

The indicator function $I(\boldsymbol{x})$ is 0 when $\boldsymbol{x}$ belongs to the upper fluid, and 1 otherwise. The following equation for $I(\boldsymbol{x})$ can be derived:

$$\nabla^2 I(\boldsymbol{x}) = \int_{\partial B} \mathrm{d}x_B \nabla \cdot \boldsymbol{n}\delta(\boldsymbol{x} - \boldsymbol{x}_B). \tag{10}$$

A smooth representation of the δ-function is required for the numerical implementation of (1), (8), and (10) (see e.g. Sarkar and Schowalter, 2001a):

$$D(\boldsymbol{x} - \boldsymbol{x}_B) = D^1(x - x_B)D^1(y - y_B), \tag{11}$$

where

$$D^1(x - x_B) = \frac{1}{4\Delta x}\left[1 + \cos\frac{\pi}{2\Delta x}(x - x_B)\right] \quad \text{for } |x - x_B| \leqslant 2\Delta x. \tag{12}$$

The approximation of the delta function is coupled with the discretization of the computational domain: as the discretization length Δx approaches zero, the approximant approaches infinity, as required of a family of regular functions approaching a delta function. This representation allows a back-and-forth coupling between the discretized front and the domain variables around it. Broadly speaking we have replaced the sharp interface separating the phases by a region of sharp variation in properties, which has a finite thickness, approximately $4\Delta x$ (Sarkar and Schowalter, 2001a). Wilson and Rallison (1999) found for channel flow of elastic liquids that as the thickness of the layer over which the elastic properties vary is increased, the instability mechanism is countered by convective effects and the growth rate is reduced. A similar effect could apply in our simulations as well. Obviously the smearing of the interface will decrease as the mesh is refined; our mesh-refinement studies indicate that this effect is small for our viscosity-stratified flow configuration and parameter range.

3.2. Finite difference

This formulation leads to a system of partial differential equations with smooth spatially varying coefficients. The front is decoupled from the underlying flow equation, and is retained only as a means for computing properties at successive time steps. Note that one may choose any suitable method for the system of equations in the computational domain. We use an MAC type operator splitting/projection finite difference method. The original method solves the system in two explicit steps. A detailed description of the method can be found in Sarkar and Schowalter (2001a).

4. Results

Relevant dimensionless parameters include the ratio m of the viscosities, dimensionless velocities u^* and v^*, dimensionless wavelength λ^*, dimensionless amplitude of the perturbation a^*, and dimensionless time t^*:

$$m = \frac{\mu_1}{\mu_2}; \quad (u^*, v^*) = \frac{(u, v)}{U_0}; \quad \lambda^* = \frac{\lambda}{d_1 + d_2}; \quad a^* = \frac{a}{d_1 + d_2}; \quad t^* = \frac{tU_0}{d_1 + d_2}, \tag{13}$$

where u, v, λ, a, and t are the corresponding dimensional quantities. We consider $m \leqslant 1$ for all our computations, unless noted otherwise. Note that $m > 1$ with n replaced by n^{-1} will result in an identical situation.

4.1. Linear stability

4.1.1. Linear growth rate

The growth rate of the amplitude of the perturbation is defined as:

$$a^* = a_0^* e^{KX^*} = a_0^* e^{Kt^*}, \tag{14}$$

where K is the dimensionless linear growth rate, a_0^* is the dimensionless initial amplitude of the perturbation, and X^* is the dimensionless downstream distance. According to our non-dimensionalization scheme, $X^* = t^*$. It should be noted that a linear growth rate was used in almost all

perturbation analyses to date. In this paper, K is determined from the initial (linear) portion of the a^* versus t^* curve. The experiments of Khomami and Su (2000) also showed that the growth rates for interface disturbance were linear. However, although the initial growth rates can be linear, non-linear effects must be considered as the amplitude grows. The limitation of the size of their channel probably prevented Khomami and Su from observing non-linear instabilities.

Fig. 2 depicts a typical evolution of the amplitude of the perturbation as a function of downstream distance. For this simulation, $m = 0.5$, $n = 4$, and $Re = 7.1$. Reynolds number is defined as $Re = \frac{U_0 d_v}{v_v}$, where U_0 is the interfacial velocity, and d_v and v_v are the thickness and kinematic viscosity respectively of the more viscous fluid. The abscissa and ordinate in Fig. 2 are non-dimensionalized with the channel thickness. We use a 64×64 grid scheme in these simulations with a dimensionless time step $dt^* = 1.1 \times 10^{-3}$. The initial dimensionless amplitude of the perturbation a_0^* is 0.0005, and the dimensionless wavelength λ^* is 0.5. The perturbation grows by a factor of ten at $t^* = 15$. It is apparent that the simulation returns a linear growth rate for $t^* < 17$. The growth rate subsequently reduces, and the amplitude of the perturbation then reaches terminal value. Li et al. (1998) observed similar saturation in amplitude growth in two-layer Couette flow. In fact, weakly non-linear analysis (Renardy, 1989) predicted such saturation for a traveling wave. Fig. 2 is typical of the results in this paper, for which the growth rate is linear from the very beginning, and we compare our results with analytical results by other authors.

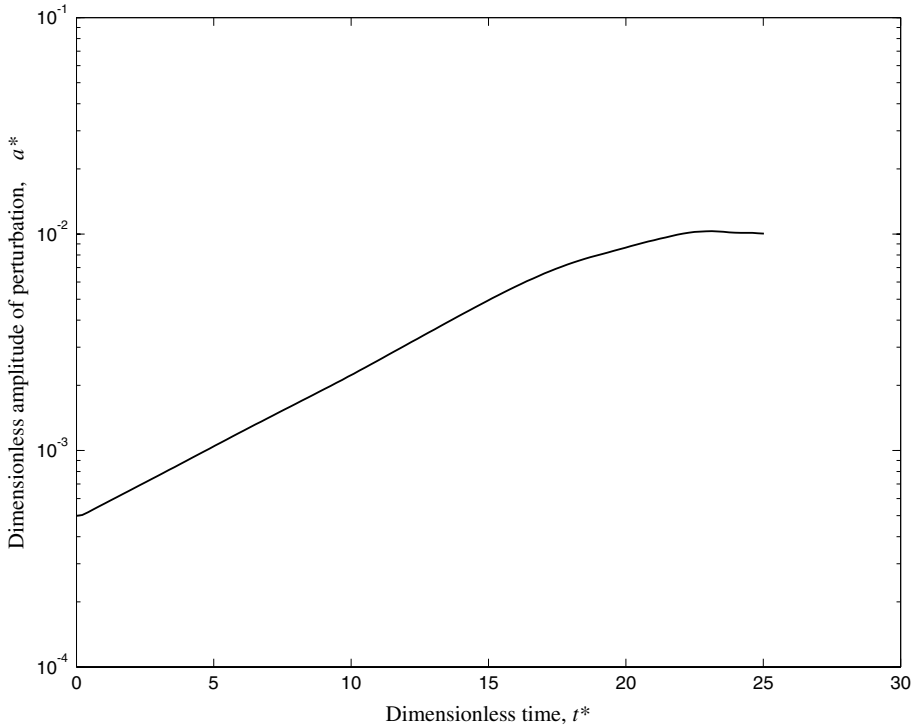

Fig. 2. Typical evolution of perturbation amplitude for $m = 0.5$, $n = 4$, $Re = 7.1$, $\lambda^* = 0.5$.

Fig. 3 shows contour plots of cross-stream velocity normalized by the interfacial velocity at different times. The parameters are the same as for Fig. 2 except that $\lambda^* = 1.0$. The x and y axes are normalized by the channel thickness. The interface location is overlaid on the plots. For a clearer view the interface displacement has been magnified by a factor of 50. As expected, the amplitude of the perturbation, and the magnitude of the vertical velocity increase with time. The largest velocities (positive and negative) occur when the interface experiences a zero crossing. The smallest vertical velocity occurs in the neighborhood of the peak displacement.

4.1.2. Code validation

We performed a grid convergence study of our code. Accordingly, three runs using different grid resolutions and time steps were performed as shown in Table 1. The parameters for the three

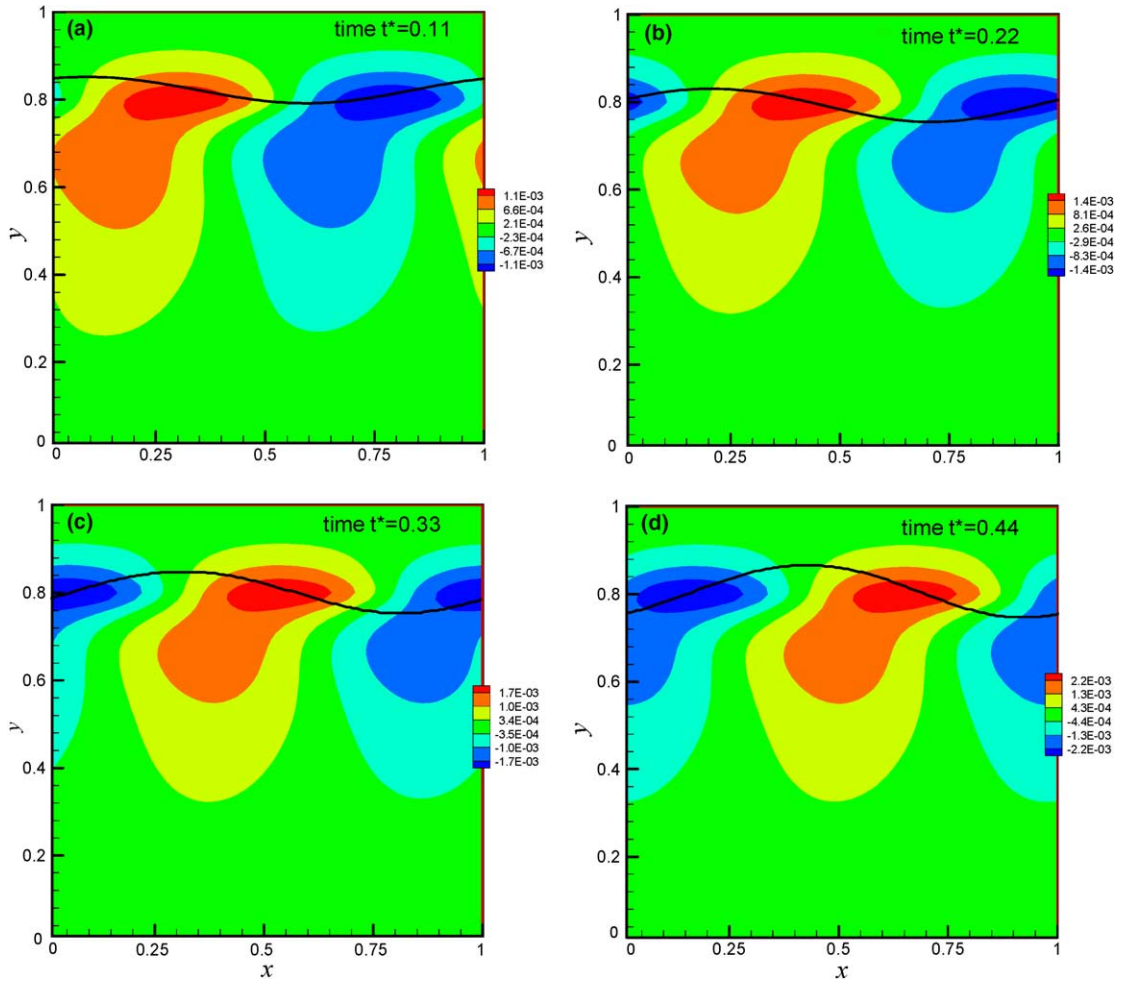

Fig. 3. Cross-stream velocity distribution for an unstable case ($m = 0.5$, $n = 4$, $Re = 7.1$, $\lambda^* = 1.0$). The interface displacement has been magnified by a factor of 50.

Table 1
Growth rates for different grid schemes and time step sizes

	Grid scheme	Dimensionless time step size	Growth rate
Case 1	64×64	2.2×10^{-3}	0.216
Case 2	128×128	5.5×10^{-4}	0.216
Case 3	64×64	1.1×10^{-3}	0.216

Table 2
Growth rates for different m and n

	m	n	Re	Growth rate
Case 1	2	0.25	7.1	0.216
Case 2	0.5	4	7.1	0.216
Case 3	2	0.333	5.4	0.210
Case 4	0.5	3	5.4	0.209

Table 3
Comparison of numerical simulation and analytical results (Khomami and Su, 2000) for two specific cases

	m	n	Re	α	Analytical growth rate	Growth rate from current numerical simulation
Case 1	0.203	3.33	0.007	0.72	0.0014	0.0014
Case 2	0.203	4.875	0.009	0.53	0.002	0.0016

cases were the same as for Fig. 2, but with $\lambda^* = 1$. Table 1 demonstrates that the growth rates for the three cases are identical.

Second, we conducted calculations with m replaced by m^{-1} and n by n^{-1}; the two cases are dynamically identical, and so our simulations should return identical growth rates. The results for two sets of calculations summarized in Table 2 confirm that this is indeed true. A third validation run was performed by setting $m = 1$; the growth rate was zero as expected. This test confirms that the two-layer simulation accurately predicts the neutral behavior of a single fluid layer, when both layers are assigned the identical viscosity.

A fourth validation was performed by running two cases using the same parameters as in the analysis of Khomami and Su (2000). We retrieve the results of two cases from their paper. For the first case, $m = 0.203$, $n = 3.33$, $Re = 0.007$, and $\alpha = 0.72$, which is the smallest wavenumber we can obtain for this case. The wavenumber is defined here as $\alpha = \frac{2\pi d_v}{\lambda}$, where d_v is the thickness of the more viscous fluid. For the second case, $m = 0.203$, $n = 4.875$, $Re = 0.009$, and $\alpha = 0.53$. The simulation results displayed in Table 3 agree reasonably well with the analytical results of Khomami and Su (2000). It may therefore be concluded that the results obtained with our front-tracking code are reliable.

4.1.3. Influence of parameters on the growth rate

Fig. 4 shows the effect of the amplitude of the perturbation on the shape of the interface. In this simulation, $m = 0.5$, $n = 4$, and $Re = 7.1$. The dimensionless wavelength is fixed at $\lambda^* = 1.0$ and different initial amplitude is applied in each case. Six curves corresponding to different time steps are plotted for each case. The dimensionless time increment is 0.533 between adjacent curves. The

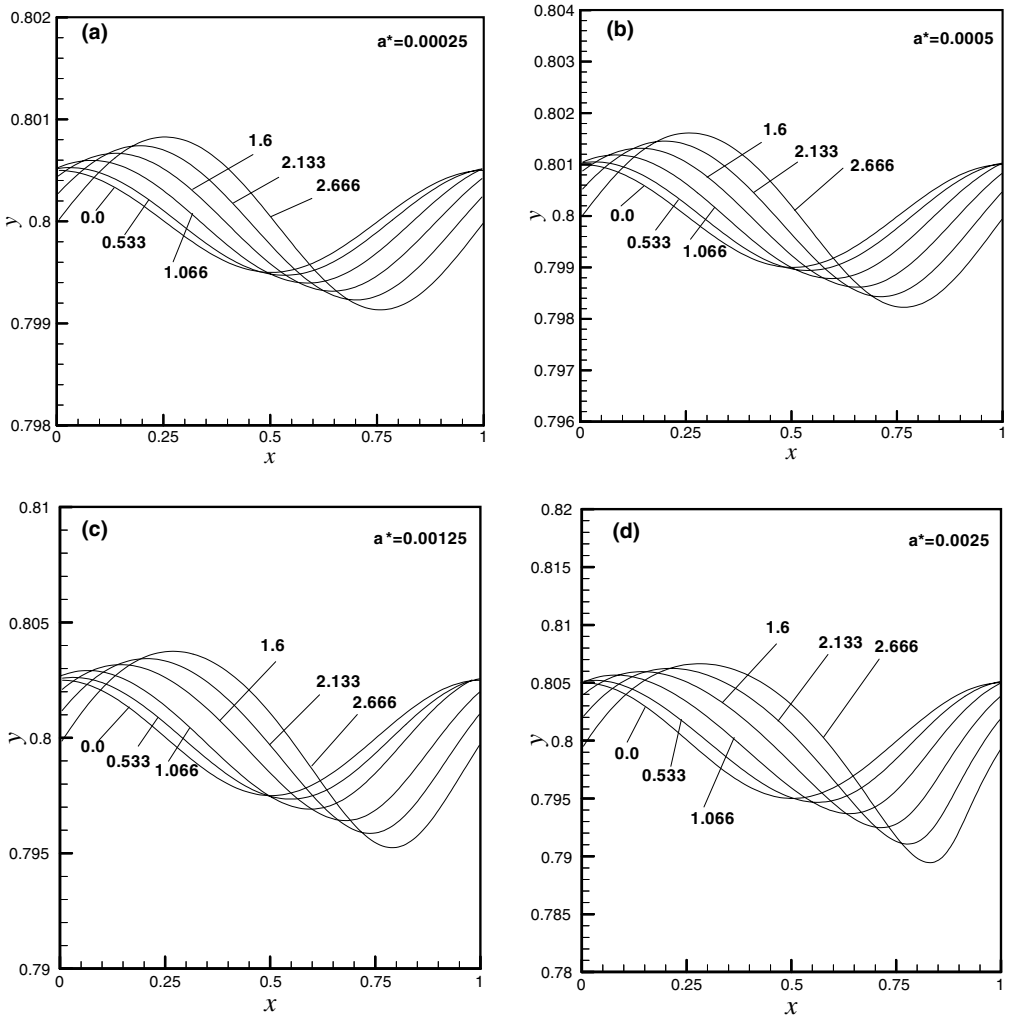

Fig. 4. The effect of initial perturbation amplitude on interface shape at different times ($m = 0.5$, $n = 4$, $Re = 7.1$, $\lambda^* = 1.0$).

interface is initially centered at $y = 0.8$. For the first plot (Fig. 4a) $a_0^* = 0.00025$. The curves are seen to be symmetric about the center of the interface, with positive and negative peaks of identical magnitude. Fig. 4b ($a_0^* = 0.0005$) does not indicate significant differences from Fig. 4a. It can be clearly observed in Fig. 4c ($a_0^* = 0.00125$) that the negative peak has grown more than the positive peak, i.e., the perturbation is now asymmetric. When a_0^* is further increased to 0.0025 in Fig. 4d, the asymmetry of the interface is more pronounced. The downstream half of the $t^* = 2.67$ curve descends much more than the other three cases and furthermore, the trough narrows to maintain identical areas above and below the interface center to conserve mass. It appears that, when the amplitude of the perturbation reaches an appreciable value, the proximity of the wall begins to express itself. Consequently, the amplitude of the positive part of the perturbation (closer to the wall) will be inhibited, and the amplitude of the negative part of the

perturbation is accentuated. Note that the amplitude of the perturbation is calculated by dividing the instantaneous peak-to-peak value by two.

The effect of Reynolds number on growth rate for different thickness ratios is shown in Fig. 5 for $m = 0.5$, and $\lambda^* = 1.0$. Fig. 5a depicts five unstable curves for thickness ratios ranging from 1.85 to 15. For $n = 1.85$, the growth rate at $Re = 0.038$ is 0.0012, and it increases in a roughly linear manner with Re to 0.152 for $Re = 38$. This is in agreement with Yih (1967) wherein a perturbation method was used to show that the growth rate for two-layer Poiseuille flow proportional to Re. At $n = 3$, a similar relationship between growth rate and Re is observed. The growth rate at $Re = 0.027$ is 0.006, whereas it is 0.211 for $Re = 10.8$. The growth rate varies linearly with Reyn-

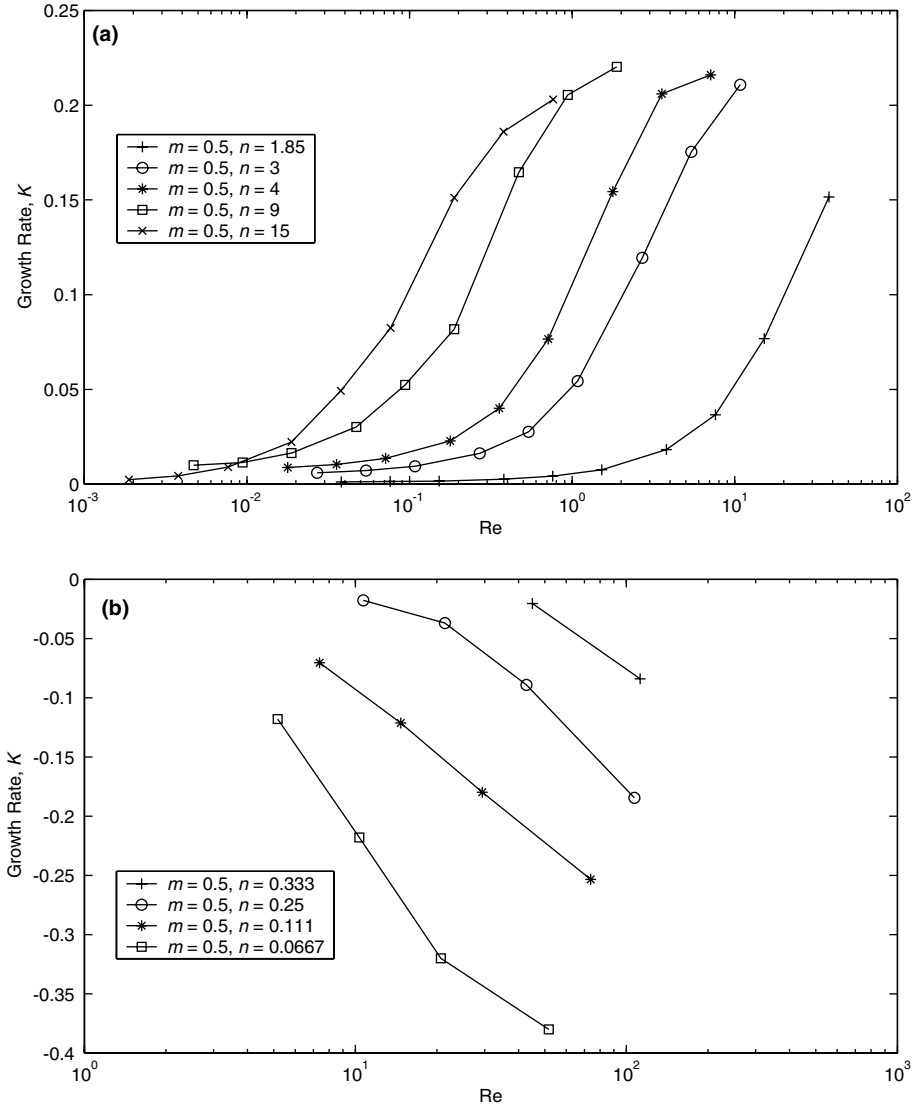

Fig. 5. Growth rate versus Re ($\lambda^* = 1.0$).

olds number when $Re \leqslant 2.7$. For $Re \geqslant 5.4$, the growth rate continues to increase with Re but at a reduced rate. Fig. 5 confirms the asymptotic analysis of Yiantsios and Higgins (1988) who stated that the neutral stability line is given by $n = \sqrt{m}$. Experiments by Cao et al. (2003) showed similar results for viscosity-stratified axisymmetric two-fluid flow; increasing Re, but with all the other parameters unchanged, indeed caused the flow to be more unstable. Fig. 5a clearly shows that the flow becomes more unstable when the thickness of the more viscous layer is reduced. One may infer therefore, that the flow may be stabilized by making the thinner layer of lower viscosity. This phenomenon has been referred to as the *thin-layer effect* (Renardy and Joseph, 1985), and it is also verified by Fig. 5b. Here, all four curves represent stable cases. The absolute value of growth rate increases almost linearly with Re. It is also shown in Fig. 5b that smaller n will stabilize the flow faster than larger n.

Fig. 6 depicts the effect of the viscosity ratio on the growth rate. Fig. 6a considers unstable cases ($n \geqslant 3$) and Fig. 6b considers stable cases ($n \leqslant 0.333$). The initial dimensionless amplitude of the perturbation is 0.0005, and $\lambda^* = 1.0$. We maintained $Re = 0.47$ for all cases in Fig. 6a. We chose $Re = 43$ in Fig. 6b because we obtained linear growth rate for only medium Re for the stable cases. When $m = 1$, the growth rate is zero, as expected. From Fig. 6a, it is obvious that the growth rate decreases with m for the cases considered here. The instability arises due to a discontinuity in the slope of the velocity profile resulting from a mismatch of viscosity at the interface between the two layers. It therefore stands to reason that the growth rate increases with viscosity difference. In addition, the flow is more unstable as n increases in agreement with Fig. 5a. Fig. 6b shows several stable cases. The growth rates are negative, except for $m = 1.0$, for which the growth rate is zero. Fig. 6b confirms the result in Fig. 5b that the flow is more stable for smaller n. It should be noted that a grid resolution of 128×128 was used to adequately resolve the thin layers corresponding to $n = 16$ and 0.0667 in Figs. 5 and 6.

In Fig. 7, we examine the interface evolution as a function of wavenumber. We use $m = 0.5$, $n = 4$ and vary λ^* to generate curves for three different Re. Specifically, for the cases of $\alpha = 0.628$, we use $L_x = 2L_y = 2(d_1 + d_2)$ and a 128×64 grid which is different from other cases. According to earlier analytical results (Khomami and Su, 2000), the critical wavenumber occurs in $1 \leqslant \alpha \leqslant 2$. The use of periodic boundary conditions in our simulations implies that we can only consider an integer number of waves in our computational box. Consequently, we are limited to discrete wavenumbers (defined in Section 4.1.2) of 0.628, 1.256, and larger values. Therefore, from Fig. 7 we can conclude that the critical wavenumber lies between 0.628 and 2.512, in agreement with Khomami and Su's (2000) result. Note that it is possible to calculate intermediate values of α by adjusting d_v, but this will cause n to vary as well and thereby preclude a proper comparison.

4.2. Non-linear cases

4.2.1. Non-linear stability

Fig. 8 shows an example of non-monotonic development of perturbation amplitude for $m = 0.5$, $n = 0.111$ and $Re = 0.47$. The resolution of the grid is increased from 64×64 to 128×128 for reliable results. The four curves in Fig. 8a correspond to four specific wavenumbers. Fig. 8b is a magnified view of 8a at the start of the computation. According to long wave analysis, all four cases are linearly stable. However, all four curves present positive slopes at first, which

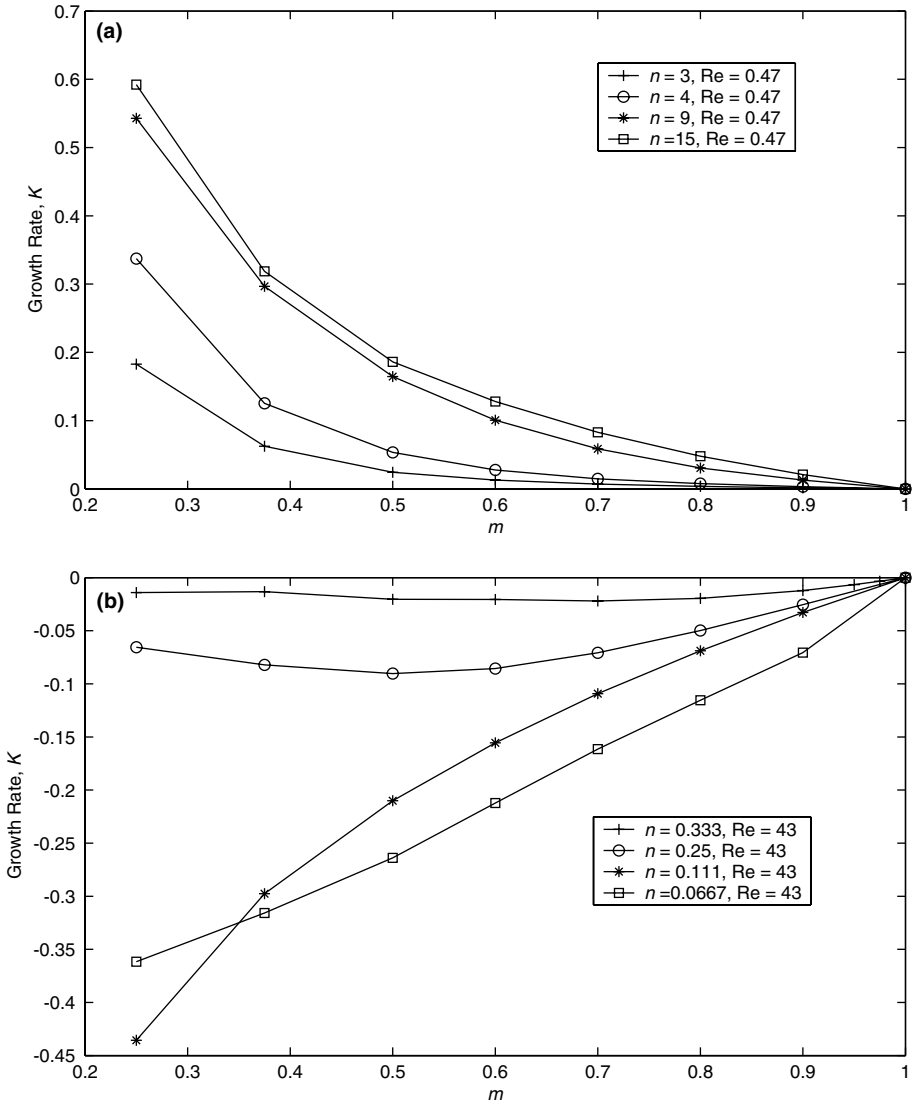

Fig. 6. Growth rate versus viscosity ratio ($\lambda^* = 1.0$). (a) Unstable cases, (b) stable cases.

suggests a tendency towards unstable behavior. [1] Renardy (1989) used methods of bifurcation theory to also show that regions previously classified as stable using long-wave analysis can in fact display unstable behavior. Although Renardy's (1989) analysis pertained to cases with interfacial tension, the departure from classical linear behavior for certain cases is replicated in our simulations. Fig. 8 shows that for all four cases, the amplitude changes in a non-monotonic fashion. For $\lambda^* = 1.0$ and 0.5, the overall trend is that the amplitude decreases, whereas for $\lambda^* = 0.25$ and

[1] Note that South and Hooper (1999) showed that certain stable mode combinations could grow transiently before decaying to zero. Two of the four cases presented in Fig. 8 ($\lambda^* = 1.0$ and 0.5) appear to belong to this category.

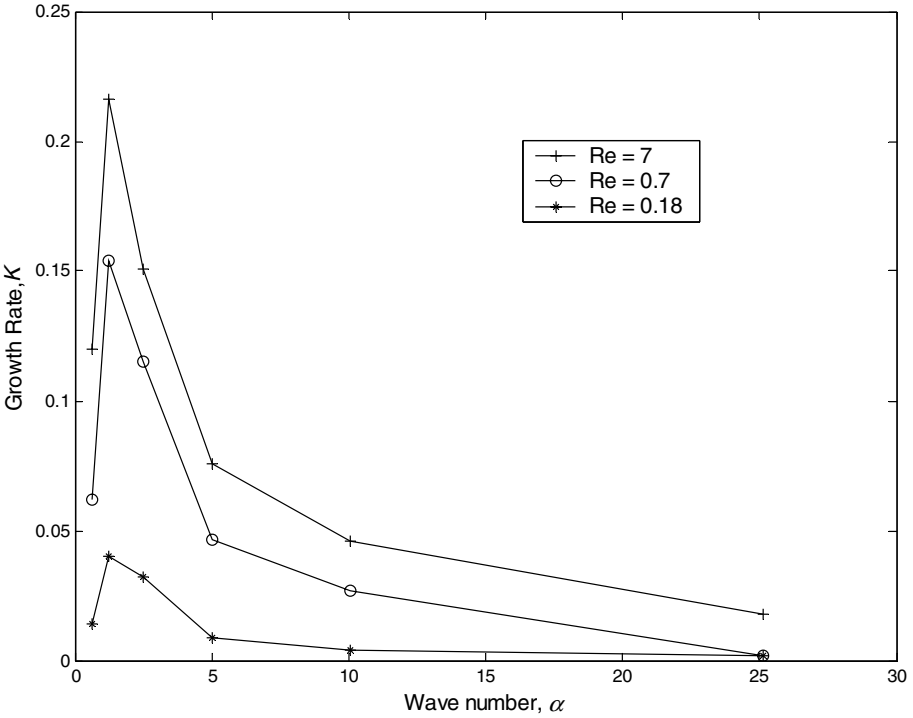

Fig. 7. Growth rate versus wavenumber ($m = 0.5$, $n = 4$).

0.125, the overall trend is that it increases. The global trend is towards more unstable behavior for smaller λ^*. Hooper and Grimshaw (1985) attributed increasing amplitude to the non-linear convective term in evolution equation, and decreasing amplitude to energy transfer to higher harmonics. They also showed that the evolution equation is stable for those wavenumbers larger than critical wavenumber. Our results indicate that the higher wavenumbers are more unstable. It appears that other non-linear mechanisms exist in addition to the energy transfer between modes. Further studies are required to resolve this issue.

4.2.2. Interface evolution in the non-linear regime

Our study was originally motivated by a strong instability observed experimentally during centerline injection of a lower viscosity jet into a higher viscosity co-flow in a tube (see Cao et al., 2003). We have been able to replicate this strong instability with our current numerical approach by starting the simulation with a sinusoidal perturbation of large amplitude ($a_0^* = 0.02$). All the simulations reported in this section were performed with a 256×256 grid. Fig. 9a presents the results from a two-layer simulation at $t^* = 3$, for $m = 0.0417$, $n = 0.0375$, $Re = 20$, and Weber number $We = \infty$. We is defined as $\frac{\rho U_0^2 d_v}{\sigma}$, where σ is the interfacial tension. For comparison, Fig. 9b presents a corresponding experimental result from Cao et al. (2003) for the same m and Re. Owing to the different geometry between experiment and simulation (axisymmetric versus two-layer respectively) the value of n in the simulation cannot exactly replicate the experimental situation. Note also, that the two liquids used in the experiments (aqueous solutions of CMC of differing

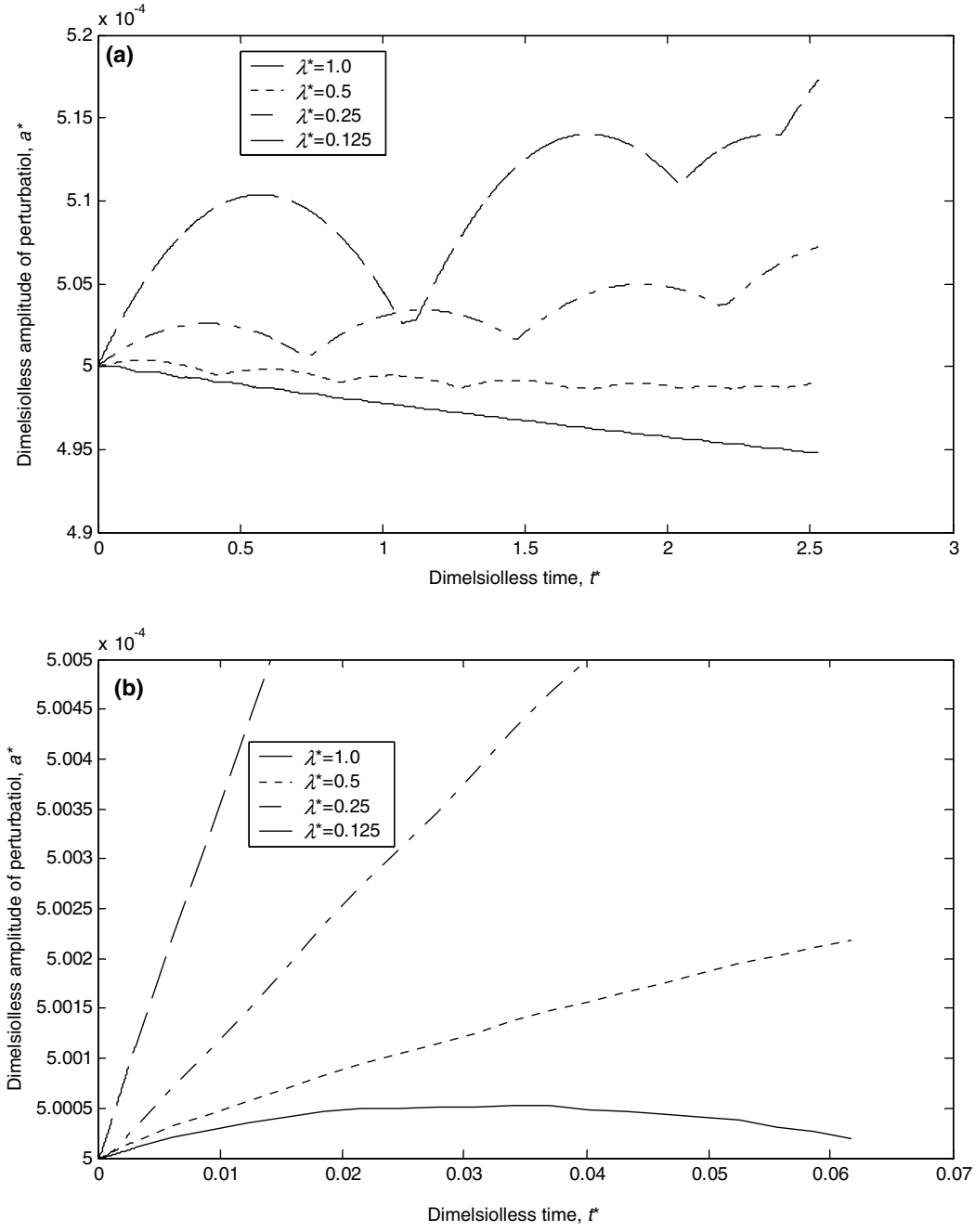

Fig. 8. Typical non-linear development of perturbation amplitude: (a) $m = 0.5$, $n = 0.111$, $Re = 0.47$; (b) magnified view of (a) at the start of the computation.

concentrations) experience a mild interfacial tension in contrast to the simulation wherein $We = \infty$ (i.e. $\sigma = 0$). Despite these differences, it is apparent that the simulation reproduces

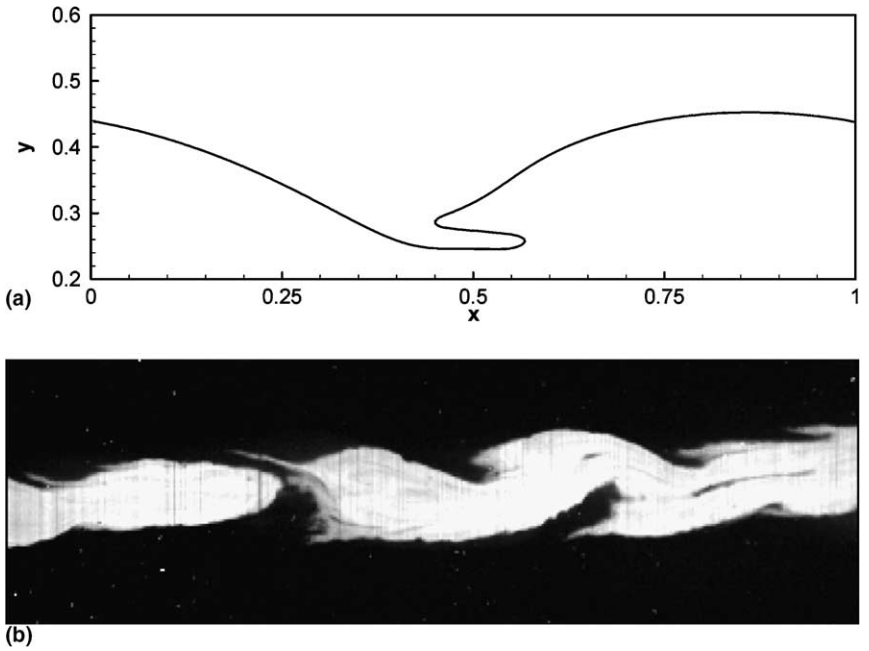

Fig. 9. Interface at $t^* = 3$ for $m = 0.0417$, $n = 0.375$, $Re = 20$, $We = \infty$. (a) Numerical result for two-layer flow; (b) experimental result for axisymmetric flow using the LIF technique (Cao et al., 2003).

features observed in the experiment such as the sharp curvature of the interface and penetrating fingers of one liquid into the other. Similar finger formation was observed by Li et al. (1998) for two-layer Couette flow using a VOF method.

Next, we studied the effect of increasing surface tension for $m = 10$, $n = 0.6$, and $Re = 5$. Fig. 10a–c depict interface positions with time for $We = \infty$, 37.5 and 18.8 respectively. As expected, decreasing We (increasing interfacial tension) causes the interface to grow less rapidly. Fig. 10a depicts a thin, highly stretched finger [2] of higher-viscosity fluid penetrating into the lower viscosity layer at $t^* = 2.8$, whereas finger development is increasingly suppressed in Fig. 10b and c for lower values of We. For these highly non-linear cases, perturbation amplitude is no longer a useful measure of interface evolution. Instead we use the front length, i.e., the actual length of the interface as our measure. Fig. 11 depicts the front length for five different We for $m = 10$, $n = 0.6$, and $Re = 5$. Increasing interfacial tension greatly impedes the growth rate of the front length. In addition, for high values of We, it is seen that the front length grows slowly at first, followed by a rapid increase. The growth rate is faster than exponential.

[2] The two-dimensional nature of the current calculations precludes the formation of a disturbance along the finger and its possible break up into drops because, unlike an axisymmetric filament, surface area for a finger represented by a two-dimensional sheet actually increases upon the superposition of a small sinusoidal undulation. Thus, a two-dimensional sheet is not susceptible to unstable capillary modes, at least for the low Re considered in this study. Drop formation was reported in a two-dimensional simulation albeit at much higher Re by Li et al. (1998); however, in their follow-up paper, Renardy and Li (1999) concluded after a mesh-refinement study that drop formation in their 2d calculation was numerical and not physical.

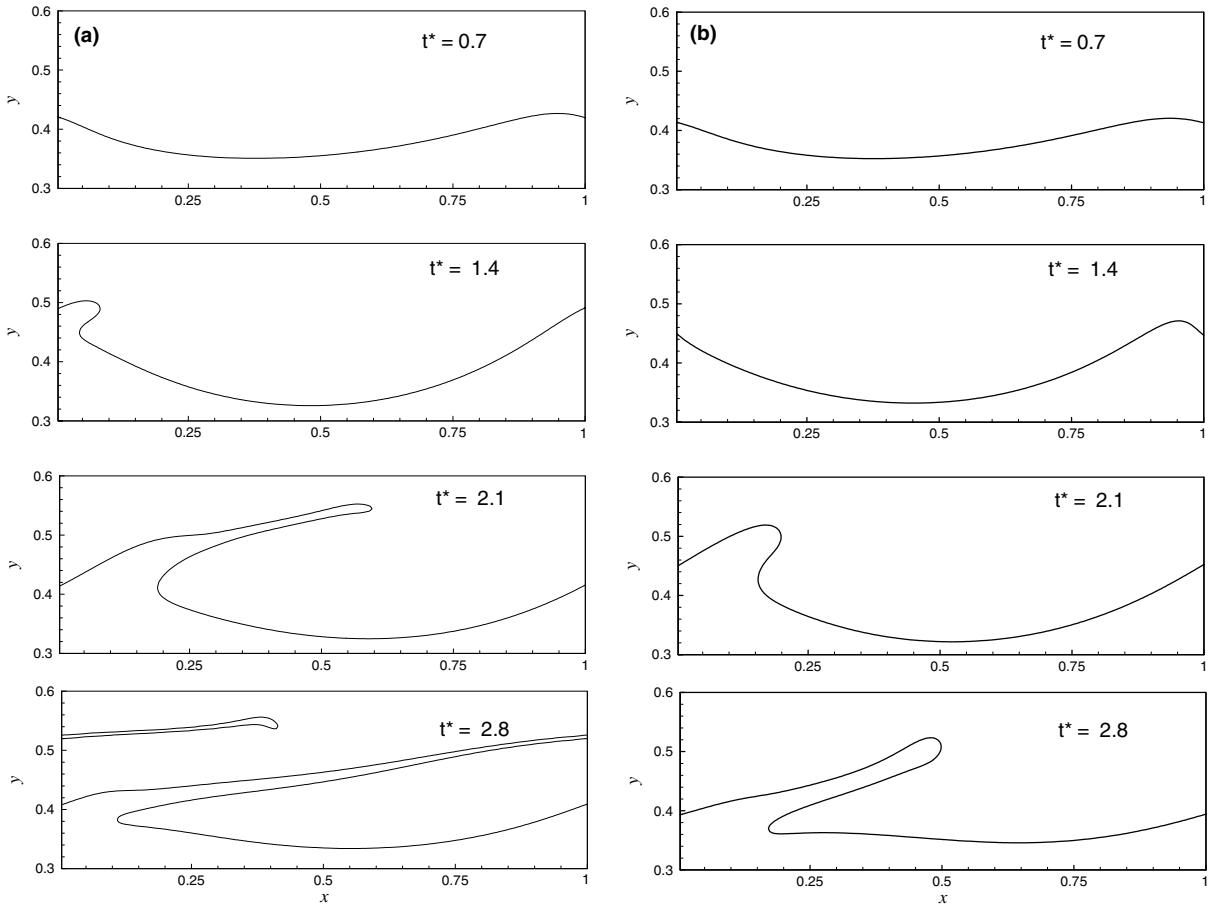

Fig. 10. Interface position at different times for $m = 10$, $n = 0.6$, $Re = 5$, and (a) $We = \infty$, (b) $We = 37.5$, (c) $We = 18.8$.

Fig. 12 depicts the interface position overlaid on streamlines for $m = 10$, $n = 0.6$, $Re = 5$, and $We = \infty$, at different times. It is apparent that the streamlines indicate mostly parallel flow even in the neighborhood of the interface for this combination of parameters. In order to accentuate the straining effect of the flow on the interface, we plot in Fig. 13 the acceleration field obtained as the difference between two flow fields centered at $t^* = 2.1$ and separated by $\Delta t^* = 0.005$. Now the stretching effect of the flow on the finger can be identified by examining the flow at the base, the tip, and the mid-finger region. The flow in the lower viscosity fluid is directed opposite to the direction of finger growth at the base, implying that the relative velocity of the finger-fluid is consistent with its penetration into the lower-viscosity layer. At the mid-finger region, the acceleration field is clearly aligned with the finger and causes it to elongate. At the tip as well, a strong elongation effect to the acceleration field is evident.

It is also interesting to observe the effect of increasing viscosity ratio m, on front development. Fig. 14 shows the front position with overlaid streamlines at different times for $m = 100$, $n = 0.6$,

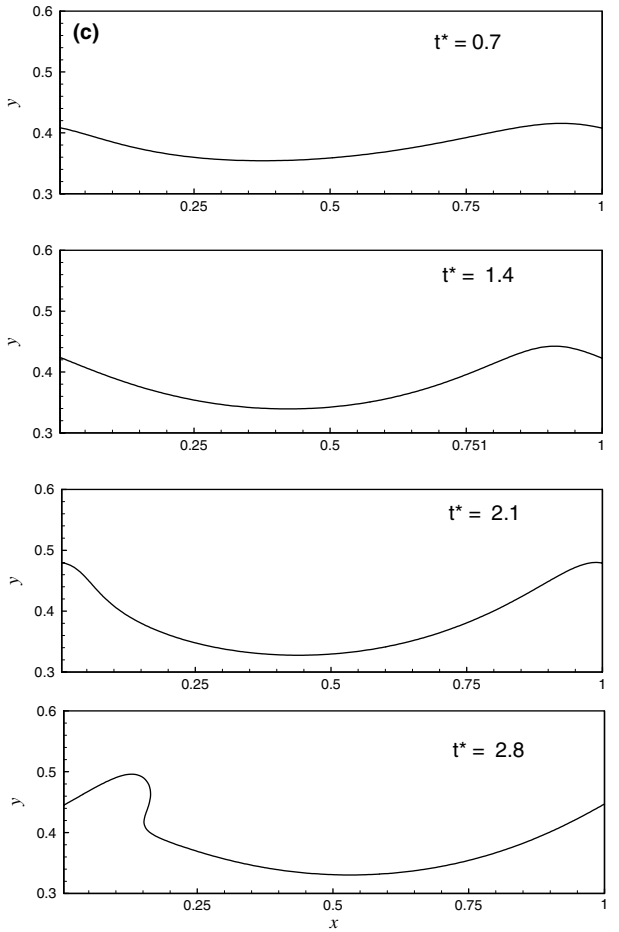

Fig. 10 (*continued*)

$Re = 5$, and $We = \infty$. It is immediately apparent that the interface develops rapidly for this high value of m; note that the finger is already well defined for $t^* = 0.2$. The streamlines now indicate that the flow is far from being parallel for this high viscosity ratio, especially in the higher viscosity layer. In fact, a region of re-circulating flow (clockwise eddy) is evident underneath the trough in the interface in the higher viscosity layer. The effect of this eddy is to pump fluid from the lower wall towards the interface just upstream of the eddy, which is consistent with the formation of a finger just upstream of this upwelling. In fact, a similar upward tilting of the streamlines can also be observed upstream of the trough in Fig. 12 form $m = 10$ (although an eddy does not form for this lower viscosity ratio).

Finally, we plot the growth of the front length with time for different m for $n = 0.6$, $Re = 5$, and $We = \infty$ in Fig. 15. It is clear that front length is strongly dependent on m, and that the front grows more rapidly for larger m. The increase in instability with m for the non-linear case is consistent with the linear results.

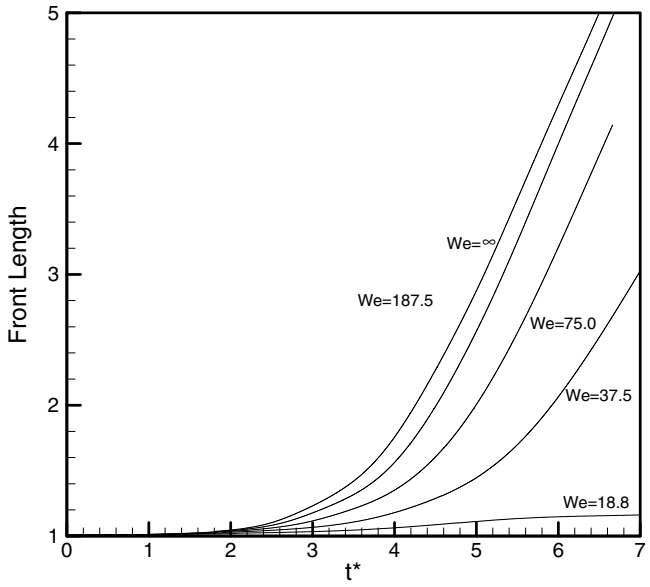

Fig. 11. Front length versus time for different We for $m = 10$, $n = 0.6$, $Re = 5$.

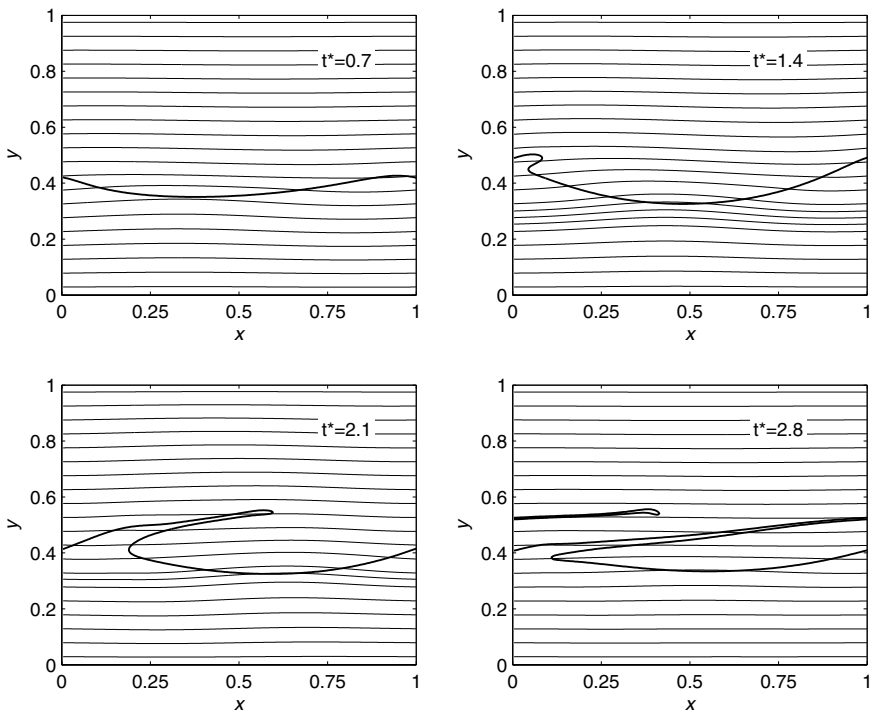

Fig. 12. Interface position and streamlines at different times for $m = 10$, $n = 0.6$, Re=5, $We = \infty$.

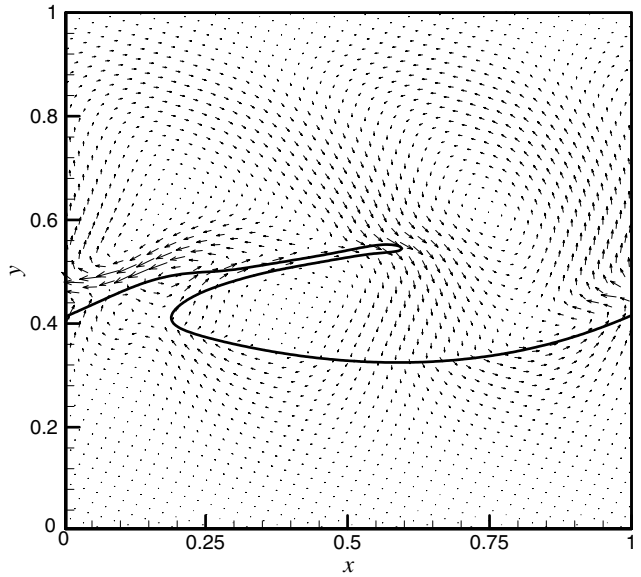

Fig. 13. Acceleration field obtained as the difference between two flow fields centered at $t^* = 2.1$ and separated by $\Delta t^* = 0.005$ for $m = 10$, $n = 0.6$, $Re = 5$, $We = \infty$.

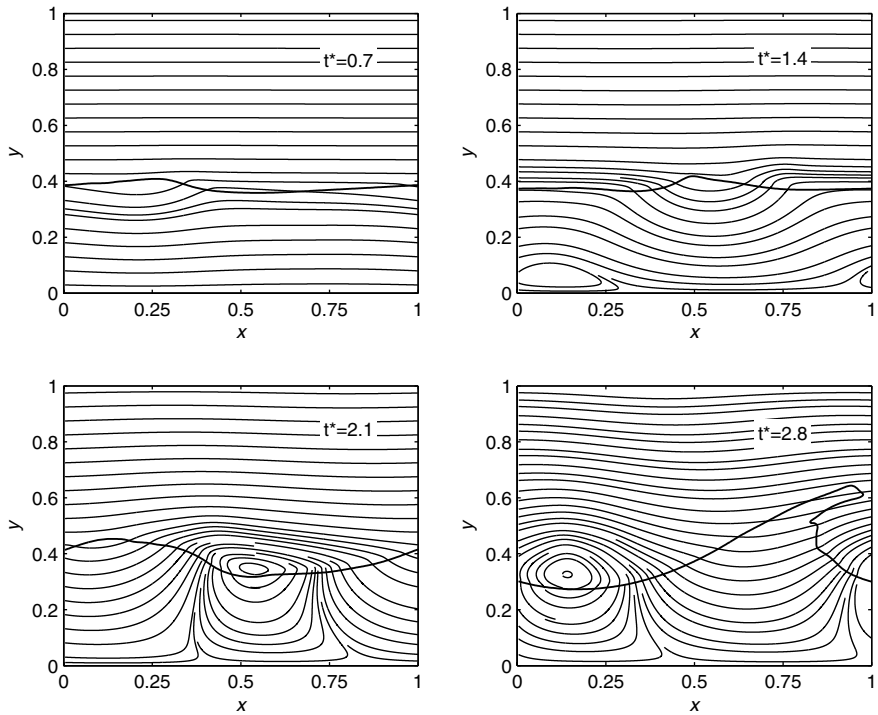

Fig. 14. Interface position and streamlines at different times for $m = 100$, $n = 0.6$, $Re = 5$, $We = \infty$.

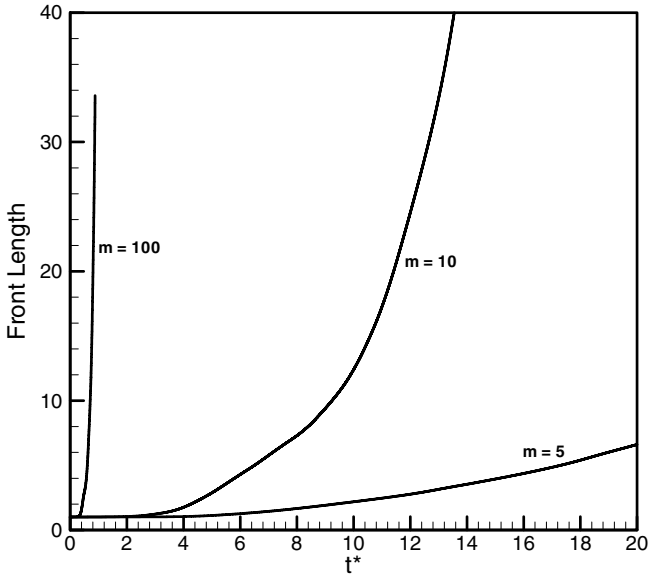

Fig. 15. Front length versus time for different m for $n = 0.6$, $Re = 5$, $We = \infty$.

5. Conclusions

We have examined two-layer density-matched viscosity-stratified Poiseuille flow using a front-tracking/finite difference method. Four computational tests were performed to validate our code and it was concluded that the front-tracking/finite difference method used here is a reliable tool to investigate interfacial instabilities. Calculations were performed at small to medium Reynolds numbers. The effects of Reynolds number, thickness ratio, viscosity ratio, and wavenumber on the growth rate of the instabilities were investigated. While the small-amplitude linear cases confirmed several theoretical predictions, the results from the large-amplitude non-linear cases are new and interesting.

For $n > \sqrt{m}$ (the unstable region in linear analysis) with small to medium Re, and $n < \sqrt{m}$ (the stable region in linear analysis) with medium Re, the growth rate of the perturbation obtained here is linear when the amplitude of the perturbation is small compared with the thickness of the channel. For $n > \sqrt{m}$ with small Re, the growth rate is proportional to Reynolds number. But for $n > \sqrt{m}$ with medium Re, the growth rate no longer increases linearly with Reynolds number but tends to slow down. Also, we show that the growth rate increases with viscosity ratio for unstable cases. The growth rate increases when the thickness of the more viscous layer is reduced. We present the effect of wavenumber on growth rate and show that the largest growth rate occurs in the region of $0.628 < \alpha < 2.512$, which is in agreement with analytical solutions.

We observe non-linear behavior in the neighborhood of the neutral curve and the region of $n < \sqrt{m}$ with small Re such that the unstable region is larger as compared with that from long wave analysis. Other non-linear mechanisms might exist in addition to energy transfer between modes.

Strong non-linear behavior is observed for large initial perturbation amplitude. The simulation replicates experimental features such as the sharp curvature of the interface and the fingers pen-

etrating from the more viscous fluid into the less-viscous layer. We examine the non-linear evolution of the interface for $n = 0.6$, and $Re = 5$ with varying m and We. Interfacial tension impedes finger development and hinders the growth of the front length greatly. The front length grows more rapidly for larger m, as was also observed for the linear case. The finger appears to initiate at a location near the crest of the interface where the streamlines are tilted upward. This phenomenon is highly evident for $m = 100$ wherein a clockwise eddy is established within the more viscous layer.

References

Cao, Q., Ventresca, A.L., Sreenivas, K.R., Prasad, A.K., 2003. Instability due to viscosity stratification downstream of a centerline injector. Can. J. Chem. Eng. 81, 913–922.

Charru, F., Fabre, J., 1994. Long waves at the interface between two viscous fluids. Phys. Fluids 63, 1223–1235.

Coward, A.V., Renardy, Y.Y., Renardy, M., Richards, J.R., 1997. Temporal evolution of periodic disturbances in two-layer Couette flow. J. Comp. Phys. 132, 346–361.

Esmaeeli, A., Tryggvason, G., 1998. Direct numerical simulations of bubbly flows. Part 1. Low Reynolds number arrays. J. Fluid Mech. 377, 313–345.

Esmaeeli, A., Tryggvason, G., 1999. Direct numerical simulations of bubbly flows. Part 2. Moderate Reynolds number arrays. J. Fluid Mech. 385, 325–358.

Hickox, C.E., 1971. Instability due to viscosity and density stratification in axisymmetric pipe flow. Phys. Fluids 14, 251–262.

Hooper, A.P., Grimshaw, R., 1985. Nonlinear instability at the interface between two viscous fluids. Phys. Fluids 28, 37–45.

Joseph, D.D., Renardy, M., Renardy, Y., 1984. Instability of the flow of immiscible liquids with different viscosities in a pipe. J. Fluid Mech. 141, 309–317.

Khomami, B., Su, K.C., 2000. An experimental/theoretical investigation of interfacial instabilities in superposed pressure-driven channel flow of Newtonian and well characterized viscoelastic fluids Part I: linear stability and encapsulation effects. J. Non-Newtonian Fluid Mech. 91, 59–84.

Khomami, B., Renardy, Y., Su, K.C., Clarke, M.A., 2000. An experimental/theoretical investigation of interfacial instabilities in superposed pressure-driven channel flow of Newtonian and well-characterized viscoelastic fluids Part II. Nonlinear stability. J. Non-Newtonian Fluid Mech. 91, 85–104.

Li, J., Renardy, Y.Y., Renardy, M., 1998. A numerical study of periodic disturbances on two-layer Couette flow. Phys. Fluids 10, 3056–3071.

Renardy, Y.Y., 1989. Weakly nonlinear behavior of periodic disturbances in two-layer Couette–Poiseuille flow. Phys. Fluids A 1, 1666–1676.

Renardy, Y.Y., Joseph, D.D., 1985. Couette-flow of 2 fluids between concentric cylinders. J. Fluid Mech. 150, 381–394.

Renardy, Y.Y., Li, J., 1999. Comment on 'A numerical study of periodic disturbances on two-layer Couette flow' [Phys. Fluids 10, 3056 (1998)]. Phys. Fluids 11, 3189–3190.

Sangalli, M., Gallagher, C.T., Leighton, D.T., Chang, H.C., McCready, M.J., 1995. Finite-amplitude waves at the interface between fluids with different viscosity—theory and experiments. Phys. Rev. Lett. 75, 77–80.

Sarkar, K., Schowalter, W.R., 2001a. Deformation of a two-dimensional drop at non-zero Reynolds number in time-periodic extensional flows: numerical simulation. J. Fluid Mech. 436, 177–206.

Sarkar, K., Schowalter, W.R., 2001b. Deformation of a two-dimensional viscous drop in time-periodic extensional flows: analytical treatment. J. Fluid Mech. 436, 207–230.

Sarkar, K., Schowalter, W.R., 2002. Computation of a free jet with embedded drops. J. Non-Newtonian Fluid Mech. 102, 263–280.

South, M.J., Hooper, A.P., 1999. Linear growth in two-fluid plane Poiseuille flow. J. Fluid Mech. 381, 121–139.

Tauber, W., Unverdi, S.O., Tryggvason, G., 2002. The nonlinear behavior of a sheared immiscible fluid interface. Phys. Fluids 14, 2871–2885.

Unverdi, S.O., Tryggvason, G., 1988. A front-tracking method for viscous, incompressible multi-fluid flows. J. Comput. Phys. 100, 25–37.

Wilson, H.J., Rallison, J.M., 1999. Instability of channel flows of elastic liquids having continuously stratified properties. J. Non-Newtonian Fluid Mech. 85, 273–298.

Yiantsios, S.G., Higgins, B.G., 1988. Linear-stability of plane Poiseuille flow of two superposed fluids. Phys. Fluids 31, 3225–3238.

Yih, C.-S., 1967. Instability due to viscosity stratification. J. Fluid Mech. 26, 337–352.

Zhang, J., Miksis, M.J., Bankoff, S.G., Tryggvason, G., 2002. Nonlinear dynamics of an interface in an inclined channel. Phys. Fluids 14, 1877–1885.